

InfScene-SR: Arbitrary-Size Image Super-Resolution via Iterative Joint-Denoising

Shoukun Sun¹, Zhe Wang², Xiang Que³, Jiyin Zhang¹, and Xiaogang Ma¹

¹ Computer Science Department,
University of Idaho, Moscow, Idaho, USA
{ssun, jiyinz, max}@uidaho.edu

² National Center for Ecological Analysis and Synthesis (NCEAS),
University of California Santa Barbara, Santa Barbara, California, USA
zwang@nceas.ucsb.edu

³ College of Computer and Information Sciences,
Fujian Agriculture and Forestry University, China
quexiang@fafu.edu.cn

Abstract. While diffusion models have achieved state-of-the-art performance in Image Super-Resolution (SR), their prohibitive computational and memory demands restrict their training and inference to fixed-size inputs. The standard workaround to super-resolve larger images relies on partitioning the image, super-resolving patches independently, and stitching them together—a process that inevitably introduces severe boundary artifacts and spatial inconsistencies in large-scale scenes. To achieve spatially continuous, arbitrary-size image super-resolution, we propose **InfScene-SR**, a diffusion-based SR approach. Building upon SR3 [20], our approach leverages Variance-Corrected Fusion (VCF) [22] to perform joint-denoising across overlapping patches. VCF guarantees continuous transitions while preserving the stochastic variance crucial for high-fidelity texture reconstruction. To overcome the prohibitive synchronization overhead of scaling joint-denoising to gigapixel imagery, we introduce Spatially-Decoupled Variance Correction (SDVC). SDVC reformulates the global fusion process into independent, atomic patch operations, drastically reducing memory complexity to $\mathcal{O}(1)$ and naturally enabling fully distributed, parallelized inference. Extensive experiments on large-scale remote sensing datasets demonstrate that InfScene-SR strictly eliminates boundary seams, achieves superior perceptual quality, and significantly boosts performance in downstream semantic segmentation task.

Keywords: Super-resolution · Diffusion Models · Large-Content Image Generation · Remote Sensing

1 Introduction

Single Image Super-Resolution (SISR) is a foundational task in computer vision, aiming to restore high-frequency details from single low-resolution observation. The applications of SISR are vast, spanning from enhancing consumer photography to critical domains like medical imaging and satellite remote sensing. While traditional methods and early CNN-based approaches [7] often produce overly smoothed results, recent

advancements have been driven by Generative Adversarial Networks (GANs) [8] and, more promisingly, Denoising Diffusion Probabilistic Models (DDPMs) [11]. Diffusion-based SR models, such as SR3 [20], formulate SR as a conditional generation process, demonstrating an unprecedented capability to synthesize photo-realistic textures and recover complex structures.

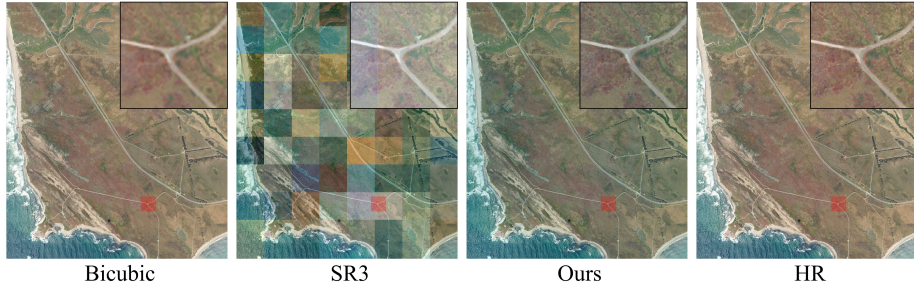


Fig. 1: Visual comparison of super-resolution methods on large-scale remote sensing imagery. The proposed InfScene-SR (Ours) reconstruction effectively eliminates the severe grid artifacts visible in the standard patch-based SR3 output, while recovering fine, high-frequency details superior to bicubic interpolation.

Despite these successes, a fundamental limitation hinders the practical deployment of diffusion-based SR models: their restriction to fixed, relatively small input patches (e.g., 512×512) dictated by the memory constraints of attention mechanisms. Real-world applications, such as medical whole-slide imaging or satellite remote sensing, routinely require the processing of arbitrary-sized, gigapixel-scale scenes. The standard engineering workaround—partitioning the large image into a grid of independent patches, super-resolving them individually, and stitching the results—often falls short for diffusion models. Because the reverse diffusion process is inherently stochastic, independently generated, contiguous patches frequently produce inconsistent content. This inevitably leads to noticeable semantic discontinuities and visible seams at patch boundaries, disrupting the spatial coherence necessary for both human interpretation and downstream analysis.

To enforce spatial continuity, recent large-content image generation methods employ joint-denoising, where creating a series of overlapping patches and fusing overlapped areas at each denoising step. However, we identify a critical issue when applying joint-denoising to diffusion-based SR models like SR3: *Variance Erosion*. Since each patch contains independent stochastic noise in Stochastic Differential Equation (SDE) solvers, averaging these overlapping areas artificially attenuates the variance of the underlying noise distribution. Over successive refinement steps, this variance collapse accumulates, progressively stripping away the high-frequency generative capability of the model and resulting in fuzzy, over-smoothed reconstructions.

To overcome these challenges, we present **InfScene-SR**, a diffusion-based super-resolution approach that enables continuous, arbitrary-size image super-resolution in

a fully parallelized manner. Motivated by recent advances in large-content text-to-image generation [22], we adopt Variance-Corrected Fusion (VCF) to restore the exact stochastic variance eroded during the joint-denoising process, ensuring the preservation of high-fidelity textures. Crucially, we reformulate the global normalization process to introduce a *Spatially-Decoupled Variance Correction (SDVC)* mechanism. By untangling the spatial dependencies between overlapping patches, SDVC allows for fully parallelized fusion.

Our contributions are summarized as follows:

- We observe that applying joint-denoising to SDE-based diffusion models (e.g., SR3) suffers from *Variance Erosion*. We address this by adapting the Variance-Corrected Fusion (VCF) strategy, effectively enabling diffusion models to perform continuous super-resolution on arbitrary-sized images.
- We mathematically reformulate the fusion process to propose Spatially-Decoupled Variance Correction (SDVC). This approach supports fully pipelined parallel computation with low memory complexity, making the super-resolution of gigapixel-level images practically feasible.
- We conduct comprehensive experiments on a highly practical real-world remote sensing task. In addition to standard image quality evaluations, we emphasize spatial continuity and demonstrate the practical utility of our method through significant performance improvements in downstream tasks like semantic segmentation.

2 Related Work

2.1 Image Super-Resolution

Deep learning has revolutionized Single Image Super-Resolution (SISR). Early methods like SRCNN [7] learned end-to-end mappings from LR to HR spaces. Subsequent architectures introduced residual blocks (ResNet) [9], dense connections (DenseNet) [12], and attention mechanisms [25] to improve reconstruction fidelity. To tackle the issue of blurry textures associated with Mean Squared Error (MSE) loss, GAN-based methods such as SRGAN [13] and ESRGAN [26] introduced adversarial losses, encouraging the generation of photo-realistic textures. Despite their success, GANs can suffer from training instability and generation artifacts.

2.2 Diffusion Models for Super-Resolution

Diffusion models have recently set new benchmarks in generative modeling. Ho et al. [11] introduced Denoising Diffusion Probabilistic Models (DDPMs), which learn to reverse a gradual noising process. Saharia et al. adapted DDPM for super-resolution in SR3 [20], conditioning the reverse process on the LR image. SR3 demonstrated that diffusion models could outperform regression and GAN-based baselines in human evaluation. Subsequent works have focused on improving sampling speed and conditioning mechanisms, but most assume fixed-size inputs.

2.3 Large-Content Image Generation

Generating or processing images beyond the training crop size is a challenge. In the context of large-content image generation, recent works have explored patch-based generation. Multidiffusion [1] proposes a multi-view fusion strategy, where overlapping patches are generated and fused at each step to generate large-content image exceed the training crop size, enforcing spatial continuity. SyncDiffusion [14] attempts to synchronize the gradient updates of each patche to ensure aligned style over large images. However, these methods have only considered the Ordinary Differential Equation (ODE) noise scheduler such as Denoising Diffusion Implicit Model (DDIM) [21]. More recently, Sun et al. [22] proposed a guided and variance-corrected fusion approach for large-content image generation. This method reserves the patch’s statistical variance of overlapping regions in the reverse process, ensuring spatial consistency and fine-grained details. Our work extends these concepts to the conditional setting of SR, enabling the arbitrary-size image super-resolution.

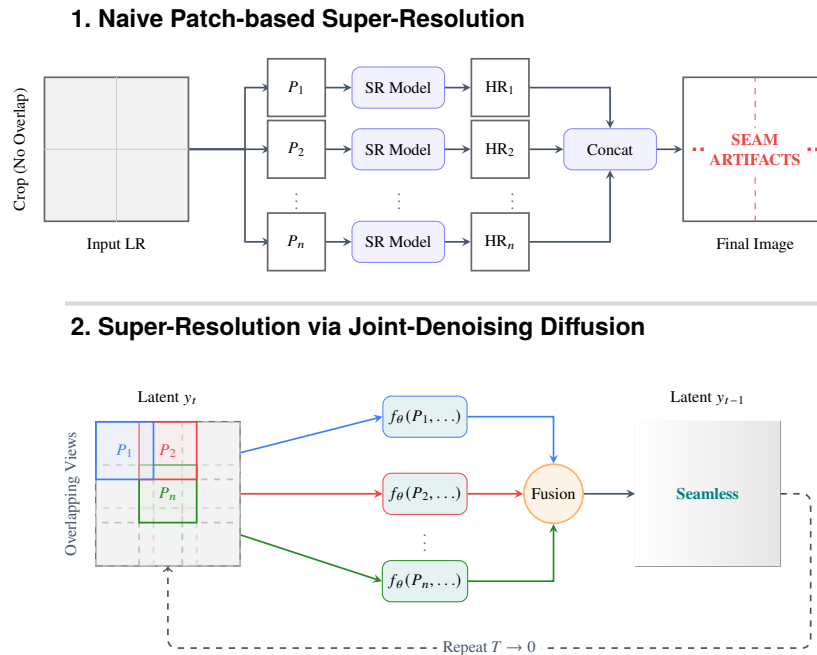


Fig. 2: Comparison of inference pipelines. Top: Naive patch-based processing leads to boundary seams. Bottom: The proposed InfScene-SR pipeline employs a joint-denoising strategy with overlapping views and a fusion mechanism to ensure global spatial continuity.

3 Proposed Method

3.1 Motivation

Super-resolving arbitrarily large low-resolution images to high-resolution remains a significant challenge. A common workaround, as illustrated in the first row of Fig. 2, is to partition a large target image into smaller patches, apply a super-resolution model to each patch independently, and concatenate the results together. However, this independent processing disrupts global spatial coherence, inevitably introducing noticeable seams and boundary artifacts.

Recent advancements in large-content image generation have demonstrated that joint-denoising—fusing a series of overlapped patches partitioned from the target image at each step of the denoising process—can mitigate these boundary artifacts and enforce spatial continuity. The Fig. 2 (bottom) illustrates the joint-denoising pipeline, which effectively eliminates boundary seams. Yet, applying joint-denoising directly to Stochastic Differential Equation (SDE) noise scheduler leads to a critical issue: unintended variance reduction during the fusion step, which causes the final outputs to be fuzzy and over-smoothed.

To address these challenges, we propose **InfScene-SR**, enabling super-resolving spatially continuous, arbitrary-sized images. By integrating a variance-corrected joint-denoising process with a conditional diffusion model and formulating a fully parallelizable inference pipeline, our approach seamlessly resolves patch boundaries without sacrificing the high-frequency details characteristic of SDE-based diffusion models.

3.2 Background: Image Super-Resolution via Iterative Refinement

We employ SR3 [20], a conditional diffusion model, as our super-resolution backbone. Let x represent the low-resolution conditioning image and y_0 represent the target high-resolution image. The forward diffusion process gradually adds Gaussian noise to y_0 over T iterations according to a variance schedule $\alpha_{1:T}$:

$$q(y_t|y_{t-1}) = \mathcal{N}(y_t|\sqrt{\alpha_t}y_{t-1}, (1 - \alpha_t)I). \quad (1)$$

During training, a neural network $f_\theta(x, y_t, \gamma_t)$, where $\gamma_t = \prod_{i=1}^t \alpha_i$ represents the cumulative noise schedule, is optimized to predict the noise ϵ added to the image. The training objective minimizes the expected denoising loss:

$$\mathcal{L}(\theta) = \mathbb{E}_{y_0, \epsilon \sim \mathcal{N}(0, I), t} \left[\left\| \epsilon - f_\theta \left(x, \sqrt{\gamma_t} y_0 + \sqrt{1 - \gamma_t} \epsilon, \gamma_t \right) \right\|_1 \right]. \quad (2)$$

During standard inference, the model iteratively recovers the signal from pure noise $y_T \sim \mathcal{N}(0, I)$ using the reverse Markov chain. At each step t , the predicted mean μ_t is computed as:

$$\mu_t = \frac{1}{\sqrt{\alpha_t}} \left(y_t - \frac{1 - \alpha_t}{\sqrt{1 - \gamma_t}} f_\theta(x, y_t, \gamma_t) \right). \quad (3)$$

The previous state y_{t-1} is then sampled by adding stochastic noise:

$$y_{t-1} = \mu_t + \sigma_t \epsilon_t, \quad (4)$$

where $\sigma_t = \sqrt{1 - \alpha_t}$ and $\epsilon_t \sim \mathcal{N}(0, I)$.

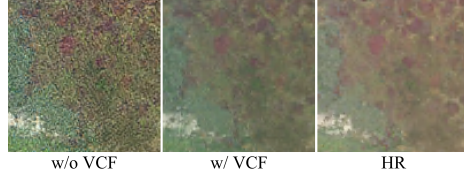


Fig. 3: Effect of Variance Erosion. Left: naive joint-denoising produces blurred output. Center: Variance-Corrected Fusion (VCF) restores sharp textures. Right: ground truth.

3.3 Variance Erosion in Joint-Denoising

To super-resolve an image larger than the model’s training capacity, we extract a set of N overlapping patches. Let $y_t^{(i)}$ and $x^{(i)}$ denote the i -th patch of the target and conditioning images at step t , respectively. During standard joint-denoising, spatial consistency is enforced by averaging the overlapping regions. We utilize a spatial weighting map w_i , where values peak at the center of the i -th patch and linearly decay to zero at the edges [22], to minimize boundary disruptions.

For a specific pixel covered by multiple patches, the naive weighted average of the sampled states $y_{t-1}^{(i)}$ is given by:

$$\hat{y}_{t-1} = \frac{\sum_{i=1}^N w_i y_{t-1}^{(i)}}{\sum_{i=1}^N w_i}. \quad (5)$$

However, because SR3 employs an SDE sampler, each $y_{t-1}^{(i)}$ contains an independent stochastic noise term $\sigma_t \epsilon_t^{(i)}$. Assuming the predicted means $\mu_t^{(i)}$ are highly correlated in the overlapping region ($\mu_t^{(i)} \approx \mu_t$), the variance of the fused pixel \hat{y}_{t-1} evaluates to:

$$\text{Var}(\hat{y}_{t-1}) = \text{Var}\left(\frac{\sum_{i=1}^N w_i (\mu_t^{(i)} + \sigma_t \epsilon_t^{(i)})}{\sum_{i=1}^N w_i}\right) = \sigma_t^2 \frac{\sum_{i=1}^N w_i^2}{\left(\sum_{i=1}^N w_i\right)^2}. \quad (6)$$

By the Cauchy-Schwarz inequality, $\sum w_i^2 < (\sum w_i)^2$ for $N > 1$. Consequently, the fused variance is strictly less than the target variance σ_t^2 . We describe this phenomenon as *Variance Erosion*. This attenuation of stochasticity accumulates over T iterations, leading to the blurry outputs characteristic of naive joint-denoising as shown in Fig. 3.

We employ the Variance-Corrected Fusion (VCF) formulation from GVCFDiffusion [22] to mathematically correct this variance collapse while preserving the guided fusion. The VCF step for the global pixel is defined as:

$$y_{t-1} = \frac{\sum_{i=1}^N w_i y_{t-1}^{(i)}}{\sqrt{\sum_{i=1}^N w_i^2}} + \left(1 - \frac{\sum_{i=1}^N w_i}{\sqrt{\sum_{i=1}^N w_i^2}}\right) \frac{\sum_{i=1}^N w_i \mu_t^{(i)}}{\sum_{i=1}^N w_i}. \quad (7)$$

This formulation guarantees that the fused pixel perfectly restores the expected target variance σ_t^2 without shifting the expected mean.

3.4 Spatially-Decoupled Variance Correction

While Eq. 7 resolves the Variance Erosion problem, it introduces a severe computational bottleneck. Calculating this formula requires gathering the predicted means $\mu_t^{(i)}$ and sampled states $y_{t-1}^{(i)}$ from all N overlapping patches into a centralized memory space and conducting global normalization computations. This synchronization overhead requires extensive use of memory and prevents efficient parallelization across distributed GPUs.

To formulate a fully parallelizable pipeline, which we name *Spatially-Decoupled Variance Correction (SDVC)*, we restructure the Eq. 7. Let W and S represent global normalization maps with the same spatial dimensions as the final large image. For any pixel coordinate p , we pre-calculate these global maps as:

$$W[p] = \sum_{j=1}^N w_j[p], \quad S[p] = \sqrt{\sum_{j=1}^N w_j[p]^2}. \quad (8)$$

By substituting global spatial matrices W and S into Eq. 7, we can algebraically expand and simplify the element-wise update for the global image:

$$y_{t-1} = \sum_{i=1}^N \frac{1}{S} w_i y_{t-1}^{(i)} + \sum_{i=1}^N \frac{S-W}{SW} w_i \mu_t^{(i)}. \quad (9)$$

Equation 9 forms the core of the SDVC pipeline. By moving the global normalization matrices W and S inside the summation, the variance-corrected fusion process becomes completely spatially decoupled. During inference, each GPU or computing node can independently calculate its patch’s localized contribution tensor $C_t^{(i)}$:

$$C_t^{(i)} = \frac{w_i}{S} \odot y_{t-1}^{(i)} + \left(\frac{S-W}{SW} \right) w_i \odot \mu_t^{(i)}, \quad (10)$$

where \odot denotes element-wise multiplication. Once computed, the independent tensor $C_t^{(i)}$ is asynchronously accumulated onto the global canvas. This eliminates the need for dense inter-node synchronization, enabling high-fidelity super-resolution of arbitrarily large sizes across a distributed computing cluster.

This reformulation yields two critical architectural advantages:

- **$O(1)$ Memory Complexity:** The inference engine is only required to maintain the memory overhead for a single patch, independent of the target image’s total resolution (H, W) . This effectively enables super-resolving ultra-large images on standard consumer-grade GPUs.
- **Operator Atomicity:** Because the localized computation of each $C_t^{(i)}$ is mathematically independent, the inference process can be distributed asynchronously. Different geographical tiles can be processed by disparate nodes and seamlessly merged via simple summation, completely removing the need for post-hoc blending or multi-patch memory synchronization.



Fig. 4: Geographic extent of the study area. The dataset covers 15 coastal counties in California using 2024 NAIP imagery, with Santa Barbara County reserved for validation and testing.

4 Experiments

4.1 Datasets

We formulate a $5\times$ super-resolution task using remote sensing imagery National Agriculture Imagery Program (NAIP) [24] to evaluate our method. Remote sensing imagery provides a particularly compelling benchmark for spatially continuous SR: geospatial analysis fundamentally operates on seamless, scene-level reconstructions rather than disjoint patches. Patch-based processing fractures spatially continuous ground objects—such as buildings, roads, and vegetation canopies—across tile boundaries. In downstream tasks that rely on the identification and delineation of these objects, such discontinuities can introduce systematic errors in both geometric and semantic accuracy.

The chosen of $5\times$ scale factor and NAIP imagery reflecting a real-world resolution gap and downstream applications. The NAIP dataset provides sub-meter 0.6 m high-resolution but is acquired only every 2–3 years, while another widely used satellite imagery, Planet [18], offers near-daily global revisits at a coarser 3 m resolution. We downsample the 0.6 m NAIP to 3 m ($5\times$) and train SR model to learn the mapping from 3 m to 0.6 m. This highlights the potential to bridge the gap: by enhancing coarse Planet observations to NAIP-level quality, continuous SR can unlock high-frequency temporal monitoring at sub-meter fidelity—a capability critical for time-sensitive applications such as agricultural phenology tracking, disaster response, and rapid land-cover change detection.

Super-Resolution Dataset The SR training data are drawn from 2024 NAIP imagery covering 15 coastal counties in California. Fig. 4 shows the extent of the training/validation/test areas, and a summary of dataset statistics is provided in Table 1. Santa Barbara County is held out for validation and testing. For the remaining 14 counties,

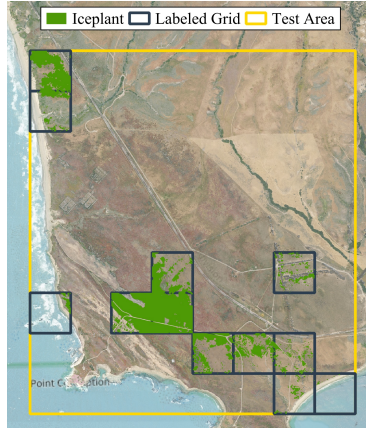


Fig. 5: Iceplant annotations on 2024 NAIP imagery. The green areas indicate the presence of Iceplant as annotated by expert ecologists.

a 10 km buffer zone extending inland from the coastline defines the extraction region; patches with less than 90% spatial overlap with the buffer zone or more than 10% invalid pixels are discarded to ensure data quality. The resulting dataset comprises 248,730 patches of size 512×512 using three spectral bands (RGB), split into 236,633 training, 8,569 validation, and 3,528 test patches.

Iceplant Segmentation Dataset To assess downstream utility, we use a semantic segmentation dataset for *Carpobrotus edulis* (Iceplant) [27] detection, an invasive species along the California coastline. This task highlights the practical value of continuous SR: NAIP’s 2–3 year revisit cycle is insufficient for tracking rapid invasive spread, whereas applying SR to daily Planet imagery could enable seasonal monitoring at sub-meter resolution. Fig. 5 shows the annotated Iceplant distribution in the test area. The dataset is located in Santa Barbara County, CA, comprising 4,913 training patches (128×128) from 2022 NAIP imagery and 261 test patches from 2024 NAIP imagery within the SR test location.

Dataset	Split	Patches	Patch Size
NAIP SR (2024)	Train	236,633	512×512
	Validation	8,569	
	Test	3,528	
	Total	248,730	
Iceplant Segm.	Train (2022)	4,913	128×128
	Test (2024)	261	

Table 1: Summary of dataset statistics. The table details the number of patches and dimensions for the NAIP Super-Resolution training set and the Iceplant segmentation downstream task.

4.2 Evaluation Framework

We evaluate our method using a comprehensive protocol that assesses pixel-level fidelity, perceptual quality, and downstream utility. A key feature of our evaluation is that it is performed on whole-image reconstructions rather than individual patches. The entire SR image of test area is generated first, and then metrics are computed on the full scene.

Pixel-wise Accuracy To measure reconstruction fidelity, we employ Root Mean Square Error (RMSE) and Peak Signal-to-Noise Ratio (PSNR). Let I_{HR} and I_{SR} denote the ground truth and super-resolved images with N pixels.

$$\text{RMSE} = \sqrt{\frac{1}{N} \sum_{i=1}^N (I_{\text{HR}}^{(i)} - I_{\text{SR}}^{(i)})^2} \quad (11)$$

$$\text{PSNR} = 10 \cdot \log_{10} \left(\frac{\text{MAX}_I^2}{\text{MSE}} \right) \quad (12)$$

where MAX_I is the maximum possible pixel value and MSE is the mean squared error. Additionally, we use the Structural Similarity Index (SSIM) [28] to evaluate structural consistency:

$$\text{SSIM}(I_{\text{HR}}, I_{\text{SR}}) = \frac{(2\mu_{I_{\text{HR}}}\mu_{I_{\text{SR}}} + C_1)(2\sigma_{I_{\text{HR}}I_{\text{SR}}} + C_2)}{(\mu_{I_{\text{HR}}}^2 + \mu_{I_{\text{SR}}}^2 + C_1)(\sigma_{I_{\text{HR}}}^2 + \sigma_{I_{\text{SR}}}^2 + C_2)} \quad (13)$$

where μ and σ represent the mean and variance of intensity, $\sigma_{x,y}$ is the covariance, C_1 and C_2 are constants to avoid division by zero.

Perceptual Quality To assess perceptual quality, we use the Fréchet Inception Distance (FID) [10] and Kernel Inception Distance (KID) [2]. Since these metrics require an Inception-v3 model [23] to extract feature embeddings, we split the whole-image into patches of size 299×299 to fit the input size of the model. We use a 75% overlap (stride of 75 pixels) moving window to extract patches, as FID and KID are distribution-based metrics whose estimates are highly sensitive to sample size [10]. The dense overlap maximizes the number of patches drawn from the test extent, yielding more stable and lower-variance metric estimates. Moreover, this overlap ensures that patch boundaries—which are the critical regions for evaluating spatial continuity—appear interior to multiple extracted patches and are therefore well-represented in the feature distribution. Both reference and SR patch sets are constructed using the same extraction procedure.

FID measures the Wasserstein-2 distance between feature distributions of HR and SR patch sets:

$$\text{FID} = \|\mu_{\text{HR}} - \mu_{\text{SR}}\|_2^2 + \text{Tr}(\Sigma_{\text{HR}} + \Sigma_{\text{SR}} - 2(\Sigma_{\text{HR}}\Sigma_{\text{SR}})^{1/2}) \quad (14)$$

where (μ, Σ) denotes the mean and covariance of features. KID calculates the squared Maximum Mean Discrepancy (MMD) between feature representations:

$$\text{KID} = \text{MMD}(f_{\text{HR}}, f_{\text{SR}})^2 \quad (15)$$

where f_{HR} and f_{SR} are the extracted features of the HR and SR patch sets, respectively. Both FID and KID are calculated using the `clean-fid` library [17], which addresses aliasing issues during image resizing.

Downstream Performance We evaluate the practical utility of super-resolved imagery through a semantic segmentation task targeting Iceplant detection. We employ a U-Net [19] architecture with a ResNet-152 [9] backbone as the segmentation model.

To generate a seamless, full-scene segmentation map, we employ a sliding window predicting strategy with significantly overlapping patches [6]. Naively stitching non-overlapping predictions often introduces blocking artifacts at patch boundaries, as convolutional networks typically exhibit degraded performance near the edges where spatial context is limited [15]. To address this, we process the full-scene input image using a patch size of $S \times S$ (where $S = 128$) and a stride of 32 pixels. A 2D Gaussian weighting window $W(i, j)$ is applied to the predicted probability map of each patch before accumulation. The weight for a pixel (i, j) within a patch is defined as:

$$W(i, j) = \exp\left(-\frac{(i - S/2)^2 + (j - S/2)^2}{2\sigma^2}\right) \quad (16)$$

where $\sigma = S/4$. This weighting creates a soft blending effect by assigning higher importance to the central pixels—where predictions are generally more reliable—and suppressing contributions from the patch edges. The final probability map P_{final} at image coordinates (u, v) is obtained by normalizing the accumulated weighted predictions:

$$P_{\text{final}}(u, v) = \frac{\sum_k P_k(u, v) \cdot W_k(u, v)}{\sum_k W_k(u, v)} \quad (17)$$

where P_k is the prediction from the k -th patch and W_k represents the Gaussian window positioned corresponding to that patch.

To comprehensively evaluate the segmentation performance, we report standard classification metrics including Accuracy, Precision, Recall, and F1 Score. Additionally, we use Intersection over Union (IoU) as a primary measure of spatial overlap:

$$\text{IoU} = \frac{\text{TP}}{\text{TP} + \text{FP} + \text{FN}} \quad (18)$$

where TP, FP, and FN represent true positives, false positives, and false negatives, respectively.

4.3 Implementation Details

SR Model Training We adopt the SR3 [20] architecture as our generative backbone, employing a conditional U-Net with channel multipliers [1, 2, 4, 8, 16], 64 base channels, group normalization with 16 groups, and a single residual block per resolution level. The network takes as input the concatenation of the low-resolution condition and the noisy image ($2C$ channels) and predicts the noise component (C channels). Weights are initialized with orthogonal initialization, and the model is trained with an L1 loss on the predicted noise.

The forward diffusion process uses a linear noise schedule with β linearly spaced from 10^{-6} to 10^{-2} over $T=2000$ timesteps. We optimize with AdamW [16] using a learning rate of 10^{-4} and weight decay of 10^{-2} . The model is trained for 100 epochs with a batch size of 8 on 512×512 patches, on two NVIDIA L4 GPUs (24 GB VRAM each), leveraging `torch.compile` and mixed-precision training (bf16) for efficiency. Low-resolution inputs are synthesized by downsampling with `cv2.INTER_AREA` to avoid spatial shifting, followed by `cv2.INTER_CUBIC` upsampling to match the target dimensions.

Iceplant Segmentation Training For the downstream semantic segmentation task, we employ a U-Net architecture with a ResNet152 backbone. The model is trained for 100 epochs with a batch size of 64. We use the AdamW optimizer with an initial learning rate of 0.01 and an ExponentialLR scheduler ($\gamma = 0.97$).

5 Results

We present the quantitative and qualitative performance of InfScene-SR compared to the standard patch-based SR3 implementation and the Bicubic interpolation baseline.

5.1 Quantitative Evaluation

Table 2 summarizes the reconstruction fidelity and perceptual quality metrics. Our results reflect the well-established perception-distortion trade-off [3]: distortion metrics like PSNR and SSIM inherently favor conservative methods that suppress high-frequency detail, while generative approaches that synthesize realistic textures are penalized despite superior perceptual quality [4, 5, 13]. Bicubic interpolation exemplifies this—as a low-pass filter, it avoids generating new content, achieving the highest PSNR (28.77 dB) and SSIM (0.7153) but the worst perceptual score (FID 90.13). Standard SR3 generates realistic textures but suffers from severe boundary artifacts via independent patching and concatenation, leading to the worst RMSE (37.05) and PSNR (16.75 dB). Our InfScene-SR significantly reduces reconstruction error compared to SR3 (RMSE from 37.05 to 24.89) while maintaining generative capability.

Most importantly, InfScene-SR achieves the best perceptual quality with the lowest FID (33.09) and KID (0.0117), demonstrating that our method produces imagery statistically closest to the real high-resolution distribution, effectively balancing structural consistency with textural fidelity.

5.2 Qualitative Comparison

Fig. 1 visually compares the methods. Bicubic interpolation produces overly smooth and blurry results, failing to resolve fine structures like vegetation texture. The standard SR3 model recovers high-frequency details but exhibits visible grid-like artifacting at patch boundaries, disrupting the visual coherence of the scene. InfScene-SR successfully synthesizes spatially continuous high-resolution details, eliminating seam artifacts while preserving the realistic textures characteristic of diffusion models.

Model	RMSE↓	PSNR↑	SSIM↑	FID↓	KID↓
Bicubic	9.2889	28.7716	0.7153	90.1341	0.0721
SR3	37.0532	16.7543	0.5783	69.3676	0.0432
InfScene-SR	24.8974	20.2077	0.6357	33.0953	0.0117

Table 2: Quantitative super-resolution evaluation. Comparison of pixel-wise fidelity (RMSE, PSNR, SSIM) and perceptual quality (FID, KID) between Bicubic, SR3, and InfScene-SR methods. The arrow symbols indicate the desired direction for each metric (lower is better for RMSE, FID, KID; higher is better for PSNR and SSIM).

Model	Accuracy↑	Precision↑	Recall↑	F1 Score↑	IoU↑
HR	0.9112	0.8365	0.8894	0.8621	0.7577
Bicubic	0.8948	0.7972	0.8892	0.8407	0.7252
SR3	0.8792	0.7982	0.8207	0.8093	0.6797
InfScene-SR	0.9101	0.8627	0.8467	0.8546	0.7461

Table 3: Segmentation performance on the Iceplant dataset. We report classification metrics (Accuracy, Precision, Recall, F1) and Intersection over Union (IoU) to assess the utility of super-resolved images for land cover mapping.

5.3 Downstream Task Performance

The practical utility of the super-resolved images is evaluated via the Iceplant semantic segmentation task (Table 3). Using original HR imagery sets the upper bound for performance with an IoU of 0.7577 and F1 Score of 0.8621.

The standard SR3 model yields the worst segmentation performance across all metrics (IoU 0.6797, Accuracy 0.8792). Its patch-boundary artifacts cause a sharp drop in Recall (0.8207), indicating that the segmentation network misses true Iceplant regions. As shown in Fig. 6, SR3 produces large contiguous false-negative (red) regions in the lower portion of the scene, where grid-like discontinuities disrupt the spatial context that the encoder relies on for vegetation delineation.

Bicubic interpolation preserves spatial continuity and thus maintains high Recall (0.8892, nearly matching HR), but its blurred textures lower Precision (0.7972) and inflate false positives (yellow regions in Fig. 6). This indicates that the over-smoothed boundaries cause the segmentation model to extend predictions beyond the true extent of Iceplant cover, resulting in over-segmentation.

InfScene-SR recovers performance nearly matching the HR upper bound, achieving an IoU of 0.7461 and F1 Score of 0.8546. Unlike Bicubic, it achieves the highest Precision (0.8627, surpassing even HR’s 0.8365), demonstrating that the synthesized high-frequency details sharpen class boundaries. Unlike SR3, it avoids the severe Recall failure by eliminating patch-boundary artifacts. The resulting error distribution in Fig. 6 closely mirrors that of HR, with residual misclassifications confined to fine boundary pixels rather than entire missed regions. This confirms that InfScene-SR’s super-resolved features are not merely perceptual hallucinations but contain semantically meaningful spectral and textural cues that enable accurate, spatially coherent land-cover classification.

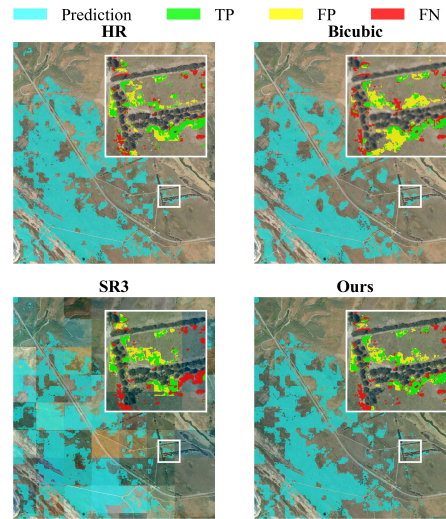


Fig. 6: Qualitative results for Iceplant segmentation. InfScene-SR (Ours) produces segmentation maps with boundary precision closer to the High-Resolution ground truth compared to other methods.

6 Conclusion

In this paper, we introduced InfScene-SR, a novel approach that extends diffusion-based super-resolution model, SR3 [20], to arbitrary-sized images. We identified that naive joint-denoising in the SR3 inference stage suffers from *Variance Erosion*, where the weighted averaging of overlapping stochastic samples suppresses the necessary variance for SDE solvers, leading to severe texture degradation. We adapted the VCF [22] to the conditional SR formulation and derived a SDVC to enable fully distributed inference. This approach resolves the variance collapse and achieves $\mathcal{O}(1)$ memory complexity, enabling high-fidelity and spatially continuous SR of gigapixel-scale imagery on consumer-grade hardware.

Extensive experiments demonstrate that our method produces spatially coherent and semantically faithful reconstructions compared with the HR image, outperforming conventional patch-stitching and interpolation baselines.

Beyond remote sensing, InfScene-SR provides a generalizable solution for other domains requiring large-scale image super-resolution, such as medical pathology and electron microscopy in material science. By enabling seamless, high-fidelity reconstructions, our approach has the potential to significantly reduce the substantial data acquisition costs across these scientific fields.

Acknowledgements

The work presented in this paper was supported by the National Science Foundation, United States (No. 2126315, No. 2428775, and No. 2514552).

References

1. Bar-Tal, O., Yariv, L., Lipman, Y., Dekel, T.: MultiDiffusion: fusing diffusion paths for controlled image generation. In: Proceedings of the 40th International Conference on Machine Learning. ICML'23, vol. 202, pp. 1737–1752. JMLR.org, Honolulu, Hawaii, USA (Jul 2023)
2. Bińkowski, M., Sutherland, D.J., Arbel, M., Gretton, A.: Demystifying MMD GANs. In: International Conference on Learning Representations (Feb 2018), <https://openreview.net/forum?id=r11UozWCW>
3. Blau, Y., Michaeli, T.: The perception-distortion tradeoff. In: Proceedings of the IEEE conference on computer vision and pattern recognition. pp. 6228–6237 (2018)
4. Chen, Y., Tai, Y., Liu, X., Shen, C., Yang, J.: Fsrnet: End-to-end learning face super-resolution with facial priors. In: Proceedings of the IEEE conference on computer vision and pattern recognition. pp. 2492–2501 (2018)
5. Dahl, R., Norouzi, M., Shlens, J.: Pixel recursive super resolution. In: Proceedings of the IEEE international conference on computer vision. pp. 5439–5448 (2017)
6. Diakogiannis, F.I., Waldner, F., Caccetta, P., Wu, C.: ResUNet-a: A deep learning framework for semantic segmentation of remotely sensed data. ISPRS Journal of Photogrammetry and Remote Sensing **162**, 94–114 (Apr 2020). <https://doi.org/10.1016/j.isprsjprs.2020.01.013>, <https://www.sciencedirect.com/science/article/pii/S0924271620300149>
7. Dong, C., Loy, C.C., Tang, X.: Accelerating the super-resolution convolutional neural network. In: European conference on computer vision. pp. 391–407. Springer (2016)
8. Goodfellow, I., Pouget-Abadie, J., Mirza, M., Xu, B., Warde-Farley, D., Ozair, S., Courville, A., Bengio, Y.: Generative adversarial nets. In: Advances in neural information processing systems. pp. 2672–2680 (2014)
9. He, K., Zhang, X., Ren, S., Sun, J.: Deep residual learning for image recognition. In: Proceedings of the IEEE conference on computer vision and pattern recognition. pp. 770–778 (2016)
10. Heusel, M., Ramsauer, H., Unterthiner, T., Nessler, B., Hochreiter, S.: Gans trained by a two time-scale update rule converge to a local nash equilibrium. Advances in neural information processing systems **30** (2017), <https://proceedings.neurips.cc/paper/2017/hash/8a1d694707eb0fe65871369074926d-Abstract.html>
11. Ho, J., Jain, A., Abbeel, P.: Denoising diffusion probabilistic models. Advances in neural information processing systems **33**, 6840–6851 (2020), <https://proceedings.neurips.cc/paper/2020/hash/4c5bcfec8584af0d967f1ab10179ca4b-Abstract.html>
12. Huang, G., Liu, Z., Van Der Maaten, L., Weinberger, K.Q.: Densely connected convolutional networks. In: Proceedings of the IEEE conference on computer vision and pattern recognition. pp. 4700–4708 (2017)
13. Ledig, C., Theis, L., Huszár, F., Caballero, J., Cunningham, A., Acosta, A., Aitken, A., Tejani, A., Totz, J., Wang, Z., et al.: Photo-realistic single image super-resolution using a generative adversarial network. In: Proceedings of the IEEE conference on computer vision and pattern recognition. pp. 4681–4690 (2017)
14. Lee, Y., Kim, K., Kim, H., Sung, M.: Syncdiffusion: Coherent montage via synchronized joint diffusions. Advances in Neural Information Processing Systems **36**, 50648–50660 (2023), https://proceedings.neurips.cc/paper_files/paper/2023/hash/9ee3a664ccfeabc0da16ac6f1f1cfe59-Abstract-Conference.html
15. Long, J., Shelhamer, E., Darrell, T.: Fully convolutional networks for semantic segmentation. In: Proceedings of the IEEE conference on computer vision and pattern recognition. pp. 3431–3440 (2015), http://openaccess.thecvf.com/content_cvpr_2015/html/Long_Fully_Convolutional_Networks_2015_CVPR_paper.html

16. Loshchilov, I., Hutter, F.: Decoupled weight decay regularization. In: International Conference on Learning Representations (2019), <https://openreview.net/forum?id=Bkg6RiCqY7>
17. Parmar, G., Zhang, R., Zhu, J.Y.: On Aliased Resizing and Surprising Subtleties in GAN Evaluation. In: Proceedings of the IEEE/CVF Conference on Computer Vision and Pattern Recognition (CVPR), pp. 11410–11420 (2022), https://openaccess.thecvf.com/content/CVPR2022/html/Parmar_On_Aliased_Resizing_and_Surprising_Subtleties_in_GAN_Evaluation_CVPR_2022_paper.html
18. Planet Labs PBC: Planet application program interface: In space for life on earth (2017), <https://api.planet.com>
19. Ronneberger, O., Fischer, P., Brox, T.: U-Net: Convolutional Networks for Biomedical Image Segmentation. In: Navab, N., Hornegger, J., Wells, W.M., Frangi, A.F. (eds.) Medical Image Computing and Computer-Assisted Intervention – MICCAI 2015, pp. 234–241. Lecture Notes in Computer Science, Springer International Publishing, Cham (2015). https://doi.org/10.1007/978-3-319-24574-4_28
20. Saharia, C., Ho, J., Chan, W., Salimans, T., Fleet, D.J., Norouzi, M.: Image Super-Resolution via Iterative Refinement. *IEEE Transactions on Pattern Analysis and Machine Intelligence* **45**(4), 4713–4726 (Apr 2023). <https://doi.org/10.1109/TPAMI.2022.3204461>, <https://ieeexplore.ieee.org/abstract/document/9887996>, conference Name: IEEE Transactions on Pattern Analysis and Machine Intelligence
21. Song, J., Meng, C., Ermon, S.: Denoising Diffusion Implicit Models. In: International Conference on Learning Representations (Oct 2020), <https://openreview.net/forum?id=St1giarCHLP>
22. Sun, S., Xian, M., Yao, T., Xu, F., Capriotti, L.: Guided and Variance-Corrected Fusion with One-shot Style Alignment for Large-Content Image Generation. *Proceedings of the AAAI Conference on Artificial Intelligence* **39**(7), 7114–7121 (Apr 2025). <https://doi.org/10.1609/aaai.v39i7.32764>, <https://ojs.aaai.org/index.php/AAAI/article/view/32764>, number: 7
23. Szegedy, C., Vanhoucke, V., Ioffe, S., Shlens, J., Wojna, Z.: Rethinking the inception architecture for computer vision. In: Proceedings of the IEEE conference on computer vision and pattern recognition, pp. 2818–2826 (2016), https://www.cv-foundation.org/openaccess/content_cvpr_2016/html/Szegedy_Rethinking_the_Inception_CVPR_2016_paper.html
24. USDA Farm Service Agency: National agriculture imagery program (NAIP) (2024)
25. Vaswani, A., Shazeer, N., Parmar, N., Uszkoreit, J., Jones, L., Gomez, A.N., Kaiser, Ł., Polosukhin, I.: Attention is all you need. *Advances in neural information processing systems* **30** (2017)
26. Wang, X., Yu, K., Wu, S., Gu, J., Liu, Y., Dong, C., Qiao, Y., Change Loy, C.: Esrgan: Enhanced super-resolution generative adversarial networks. In: Proceedings of the European conference on computer vision (ECCV) workshops, pp. 0–0 (2018)
27. Wang, Z., Halpern, B., Galaz Garcia, C.: Mapping and Monitoring the Spatiotemporal Spread of Invasive Iceplant (*Carpobrotus edulis*) Using Deep Learning and Remote Sensing Data. In: AGU Fall Meeting Abstracts. AGU Fall Meeting Abstracts, vol. 2024, pp. B11N–152 (Dec 2024)
28. Wang, Z., Bovik, A., Sheikh, H., Simoncelli, E.: Image quality assessment: from error visibility to structural similarity. *IEEE Transactions on Image Processing* **13**(4), 600–612 (Apr 2004). <https://doi.org/10.1109/TIP.2003.819861>, <https://ieeexplore.ieee.org/document/1284395>